Research Article

Wang Ya-bin, Ma Yang-fan, Zhang Qian, Zhou Yan, Ma Ting, Shi Yu*, and Zeng Min*

Numerical study on flow and heat transfer performance of a spiral-wound heat exchanger for natural gas

https://doi.org/10.1515/phys-2023-0189
received November 04, 2023; accepted January 12, 2024

Abstract: The spiral-wound heat exchanger is a key equipment in the liquefied natural gas application, but the flow and heat transfer mechanisms remain unclarified. In this study, a three-dimensional numerical model is created, focusing on exploring the impact of four crucial structural parameters on the flow and heat transfer performance of natural gas, including the external diameter of tubes, the diameter of the core cylinder, the longitudinal pitch of tubes in the same layer, and the radial pitch of tube bundles between the adjacent layer. It was found that the tube diameter, core cylinder diameter, and radial pitch had significant effects on Nu and Δp_{m}. The optimal Nu on the shell side was obtained at medium core cylinder size. The longitudinal pitch had a weak effect on the performance of both sides, and the longitudinal pitch corresponding to the maximum values of Nu and Δp_{m} on both sides increased with the increase in the inlet Reynolds number. Under the effect of centrifugal force, a shifted tendency was shown by the velocity and temperature fields.

Keywords: liquefied natural gas, spiral-wound heat exchanger, flow, heat transfer, numerical simulation.

*** Corresponding author: Shi Yu,** School of Intelligent Computing Engineering, Tianjin Renai College, Tianjin 301636, China, e-mail: shiyu234@163.com
*** Corresponding author: Zeng Min**, Key Laboratory of Thermo-Fluid Science and Engineering, MOE, Xi'an Jiaotong University, Xi'an 710049, China, e-mail: zengmin@mail.xjtu.edu.cn
Wang Ya-bin, **Zhang Qian**, **Zhou Yan:** China Petroleum Engineering & Construction Corporation, Beijing 100120, China
Ma Yang-fan, **Ma Ting:** Key Laboratory of Thermo-Fluid Science and Engineering, MOE, Xi'an Jiaotong University, Xi'an 710049, China

1 Introduction

With global economic development and population density growth, energy demand has been increasing by 0.6–1.5% per year since 2015 [1]. To address the growing challenges of climate change and the depletion of fossil fuels, ambitious energy and climate targets have been set at both national and global levels [2], and clean energy is highlighted as a main measure to achieve targets. The main component of natural gas is methane, which is widely used because of its advantages of clean and efficient combustion, reliable and durable supply, easy storage, and transportation. It has also become the fastest growing primary energy source. During medium and long-distance transportation, gas is often converted into liquefied natural gas (LNG). The most important piece of heat transfer equipment in a baseload LNG unit is the main cryogenic heat exchanger for natural gas cooling, condensation, and liquefaction [3]. The liquefaction process accounts for more than 40% of the input cost of LNG in the whole stage from production to user consumption [4]. In a natural gas liquefaction plant, the direct investment of the main low-temperature heat exchanger accounts for about 30% of the total investment cost of the liquefaction process, and the energy consumption caused by the energy loss of the main heat exchanger accounts for about 25% of the total energy consumption of the liquefaction process [5]. Therefore, the accurate design of the main heat exchanger is of great significance for reducing the investment cost, energy conservation, and emission reduction. At present, spiral-wound heat exchanger (SWHE) has shown a good application prospect in the field of LNG [6]. Therefore, it is of great importance to investigate the internal flow heat exchanger performance of SWHE for LNG.

Researchers are mostly looking at the flow and heat transfer of the working medium in the winding pipe when it comes to the secondary flow, the single-phase flow, and the gas-liquid two-phase flow of the normal working medium right now. Lei and Bao [7] analyzed the influence

of secondary flow and buoyancy effects on thermal performance under different operating conditions and structural parameters. They proposed the laminar mixed convective heat transfer prediction correlation formula for supercritical RP-3 in spiral-winding tubes. Santini *et al.* [8] experimentally studied the forced convection boiling heat transfer of water in a full-size spiral-wound tube steam generator. Wu *et al.* [9] discussed the distribution characteristics in the gas-liquid two-phase tubes and the influence of structural parameters on the boiling heat transfer process of the working medium in the winding round tube bundle, considering the effects of viscous force, centrifugal force, and gravity. Wu *et al.* [10] explored the heat transfer coefficient, secondary flow pattern, and circumferential temperature distribution of the tube cross section. Chang *et al.* [11] discussed the wall temperature distribution and heat transfer coefficient by investigating the thermal-hydraulic characteristics of supercritical water with a high mass flow rate in a vertical spiral tub. Chang *et al.* [12] fitted the corresponding flow boiling heat transfer correlation formula for different flow patterns, introduced structural parameters and heating conditions, and achieved good prediction effect. Jayakumar *et al.* [13] pointed out that a suitable model could not be generated by specifying boundary conditions with constant temperature or constant heat flow for practical heat exchangers and proposed a heat transfer correlation formula considering convection heat transfer of working medium on both sides and heat conduction at a solid wall. Mirgolbabaei *et al.* [14] discussed the influence of Reynolds number, the radius ratio of winding coil to pipe, and the dimensionless pitch ratio on forced convection heat transfer of water on both sides of vertical spiral tubes. Genić *et al.* [15] put forward the correlation formula of water heat transfer with hydraulic diameter of shell side as characteristic length when Reynolds number is 1,000–9,000. Lu *et al.* [16] found that multi-layer heat exchange tube winding has better heat transfer performance, and fitted the correlation between flow and heat transfer with Reynolds number in the range of 1,500–5,500. Haskins and Ei [17] investigated the flow loss on the shell side under adiabatic conditions by numerical simulation, and friction coefficient correlations were fitted to the obtained data for a large range of Reynolds numbers, with an error within ±6%. Zachár [18] studied the SWHE natural convection outside the tube and the heat transfer in the tube flow. The numerical simulation results of the tube-side heat transfer were compared with the experimental results and empirical formulas to verify the reliability of the numerical simulation, and it was found that the flow was in a laminar state for the natural convection on the shell-side. For boiling on the shell side of SWHE, the dryness of the working medium gradually increases, and the gas-phase shear effect and liquid wettability change of two-phase fluid lead to more complex heat transfer and pressure drop characteristics than single-phase fluid flow [19–21]. Neeraas *et al.* [22] tested the heat transfer characteristics of liquid falling-film flow for hydrocarbons and corresponding mixtures at Reynolds numbers ranging from 500 to 8,000 and recommended the Bays and McAdams correlation equation [23] to predict heat transfer properties. Ding *et al.* [19] took propane as the experimental working medium and established a shell side two-phase flow heat transfer and pressure drop correlation equation explicitly related to operating parameters and pipe pitch.

However, regarding the research of flow and heat transfer characteristics in SWHE, the current literature focuses on simple working mediums such as water, air, and pure refrigerant, with few studies on LNG. Due to the large number of grids needed to carry out numerical research on SWHE, most studies adopt thermal boundary conditions such as constant wall temperature or constant heat flux to explore the influence of structural parameters

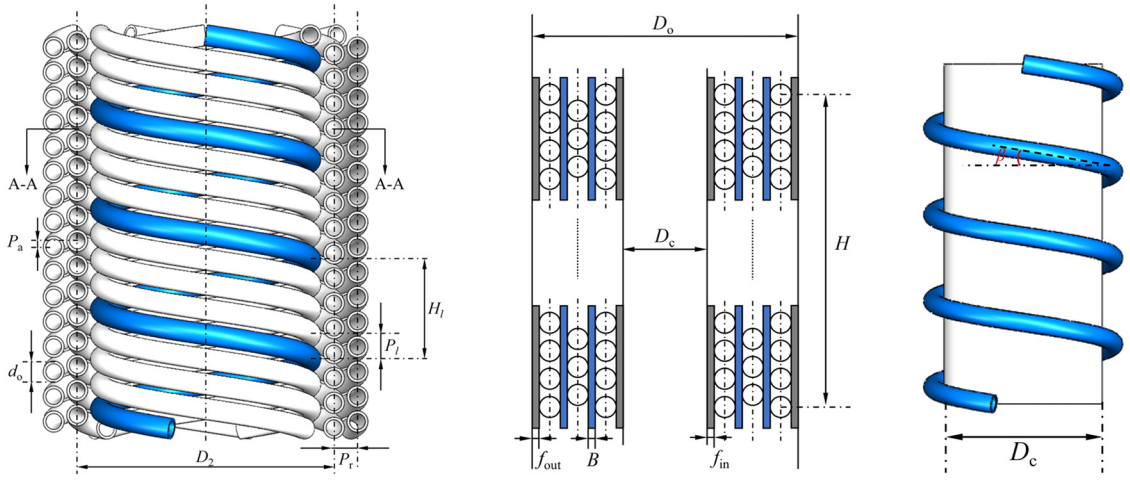

Figure 1: Axial section of SWHEs and schematic diagram of a single tube.

Table 1: Structural parameters of SWHE

Parameters (mm)	Value
d_o	10–16
D_c	70–280
P_l	19–25
P_r	18–24
f_{in}	2.0
f_{out}	2.0
n	15
H	450

on single-side flow and heat transfer characteristics, and the actual influence of LNG on both sides is still unclear. A three-dimensional numerical model was created in this work to investigate the impact of four critical structural characteristics on natural gas flow and heat transfer performance.

2 Physical model and numerical method of SWHE

2.1 Physical model

Figure 1 shows the axial profile of SWHE and the local schematic diagram of a single spiral tube, in which the structural parameters include the outer diameter of the heat exchange tube (d_o), the axial distance of the heat exchanger tube (HEB) in the same layer (P_l), the winding pitch of HEB (H_l), the radial distance of HEB in adjacent layers (P_r), the axial distance of HEB in adjacent layers (P_a), the core tube's diameter (D_c), and the outer diameter of the shell (D_o). f_{in} represents the clear distance between the innermost HEB and core wall surface, f_{out} refers to the clear distance between the outermost HEB and shell wall surface, and the winding angle is β.

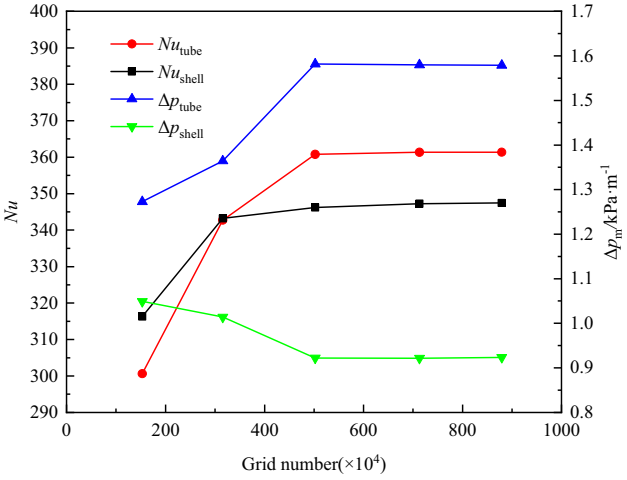

Figure 3: Grid independence test.

The winding diameter of the tube bundles in different layers is represented as D_i (i = 1, 2, 3), where the subscript i denotes the layer number. The corresponding number of winding round tubes in each layer is N_i, and their relationship can be expressed as follows:

$$\pi D_i \cdot \tan\beta = P_l N_i, \tag{1}$$

$$D_i = D_c + 2f_{in} + 2(i-1)P_r + d_o, \tag{2}$$

$$\tan\beta = \frac{P_l N_i}{\pi[D_c + 2f_{in} + 2(i-1)P_r + d_o]}. \tag{3}$$

2.2 Numerical model

This study focuses on a three-layer SWHE with an effective axial heat transfer height of 450 mm. The basic structural parameters are listed in Table 1. The remaining parameters

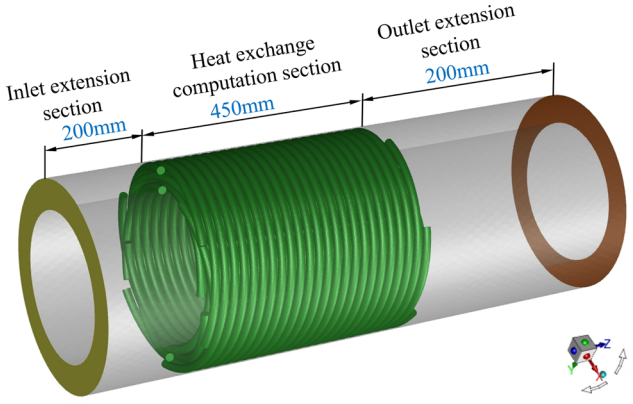

Figure 2: Numerical model.

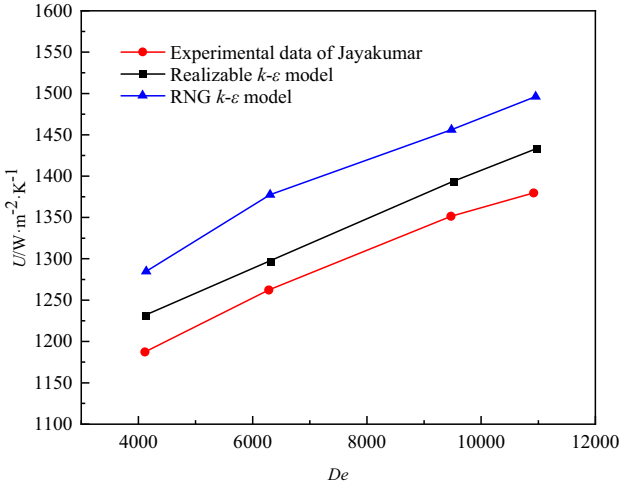

Figure 4: Model validation.

that are not listed, such as the winding diameter of the second- and third-layer heat exchange tubes, can be calculated by deducing the basic structural parameters. To make this simulation more stable, an extension section is added to the inlet and outlet regions along the axial flow direction of the shell-side working medium. The length of the extension section is 200 mm for the inlet and 450 mm for the outlet, as shown in Figure 2. In this study, it is assumed that the heat transfer within the heat exchanger occurs as a steady-state process with excellent heat preservation of the outer wall of the heat exchanger cylinder. Meanwhile, the natural convection phenomenon is caused by the change in fluid density on both sides and the heat loss to the outside world. In addition, this study does not consider

Table 2: Geometric models of external tubes with different diameters

Parameters	Geo1	Geo2	Geo3	Geo4
d_o (mm)	10	12	14	16
D_c (mm)	140	140	140	140
P_l (mm)	13	15	17	19
P_r (mm)	12	14	16	18
β (°)	6.63	7.39	8.10	8.77

the heat conduction between the gasket between the tube layers and the tube wall surface and the influence on the heat transfer characteristics of fluid flow on the shell side. The corresponding axial distance between the tube layers and the tubes in the same layer is maintained.

2.3 Numerical method

The turbulence model of this study is the realizable k–ε model with scalable wall functions, and continuity, momentum, and energy conservation equations are adopted as the governing equations.

Continuity equation:

$$\frac{\partial \rho}{\partial t} + \frac{\partial}{\partial x_i}(\rho \overline{u_i}) = 0. \tag{4}$$

Momentum equation:

$$\frac{\partial}{\partial t}(\rho \overline{u_i}) + \frac{\partial}{\partial x_i}(\rho \overline{u_i}\overline{u_j}) = \frac{\partial}{\partial x_i}(\sigma_{ij}) - \frac{\partial \overline{p}}{\partial x_i} - \frac{\partial \tau_{ij}}{\partial xj}. \tag{5}$$

Energy equation:

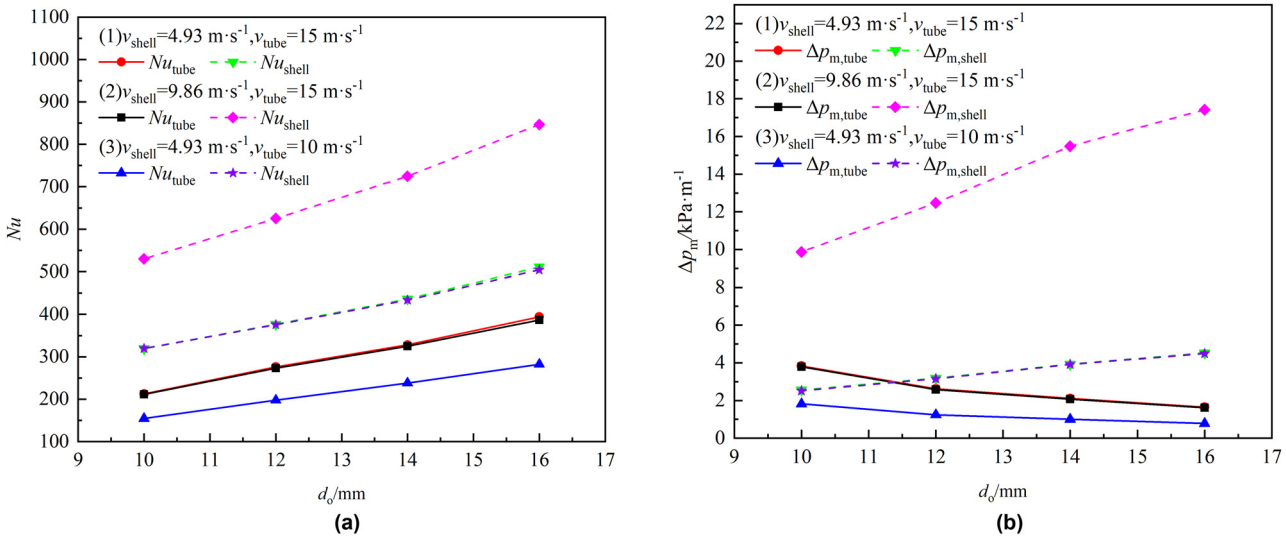

Figure 5: (a) Nu and (b) Δp_m on tube and shell sides with different external tube diameters.

$$\frac{\partial \rho \overline{h_S}}{\partial t} + \frac{\partial \rho \overline{u}_i \overline{h_S}}{\partial x_i} - \frac{\partial \overline{p}}{\partial t} - \overline{u}_j \frac{\partial \overline{p}}{\partial x_i} - \frac{\partial}{\partial x_i}\left(\lambda \frac{\partial \overline{T}}{\partial x_i}\right) = -\frac{\partial}{\partial x_j}[\rho(\overline{u_i h_S} - \overline{u}_i \overline{h_S})]. \quad (6)$$

ANSYS FLUENT software is used to solve the numerical simulation. The second-order upwind scheme is applied to discretize energy and momentum equations, and the SIMPLE algorithm is used to solve them. The inlet velocity and pressure outlet conditions are applied to the tube side. The inlet velocity is between 10 and 15 m/s with an inlet temperature of 298.15 K. The shell-side inlet uses a mass-flow-inlet boundary condition with a mass flow rate ranging from 0.755 to 4.077 kg/s and an inlet temperature of 255.15 K. The pressure-outlet boundary condition is set to the outlet of the shell side. The other wall surfaces that were not mentioned, such as the outer wall of the shell and the core wall, *etc*., were determined to be the non-slip adiabatic wall.

On both the shell and tube sides of SWHE, the fluid is the gas phase working medium of the natural gas. The components of the two working mediums are different. Considering that the thermal properties of the working medium, including density, specific heat, viscosity, and thermal conductivity, remain constant with pressure, this study establishes polynomial function relationships between the thermal properties of the working medium and temperature on both sides of the shell. The material of the tube is carbon steel with a wall thickness of 2 mm, with a specific heat capacity of 434 J kg^{-1} K^{-1} and a thermal conductivity of 45 W m^{-1} K^{-1}.

2.4 Grid independence test and model validation

In this study, unstructured polyhedral mesh division was adopted for all numerical simulation areas. Figure 3 shows the test results of grid independence, the change in Nu on both sides is less than 0.352%, and the change in Δp_m is less than 0.163% when the grid number is beyond 5,022,936. For the sake of simulation efficiency and accuracy, a grid number of 5,022,936 was chosen to discretize the geometric model in the subsequent research.

In order to verify the turbulence model adopted in this study, simulations were conducted with the same geometric structure and working parameters as in the study by Jayakumar *et al.* [13], and the working medium was water. Figure 4 displays the comparison between different turbulence models and experimental data reported in the study by Jayakumar *et al.* [13]. It is evident that the variation pattern of the total heat transfer coefficient with the Dean number aligns with the experimental results presented in the study by Jayakumar *et al.* [13]. And the calculated results of the realizable k–ε model are closer to the experimental data, with an error less than 4.0%. Therefore, the realizable k–ε turbulence model is chosen.

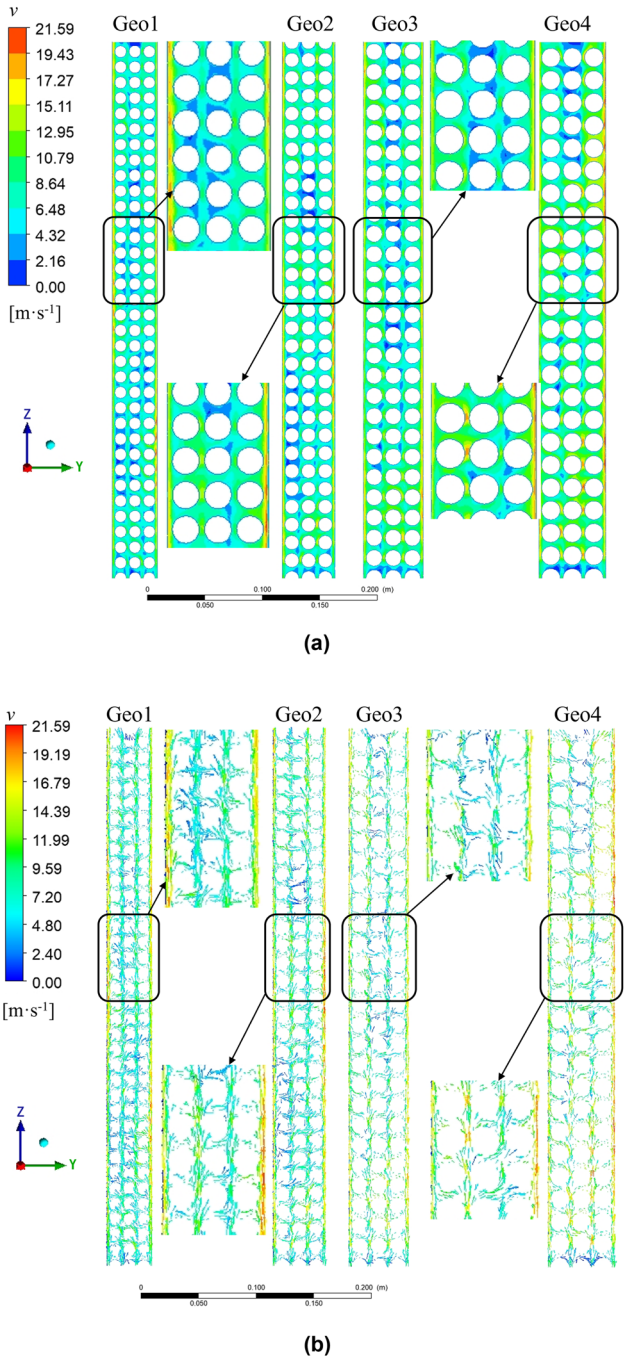

Figure 6: (a) Velocity and (b) velocity vector distributions of the shell side on the *XZ* section with different external tube diameters.

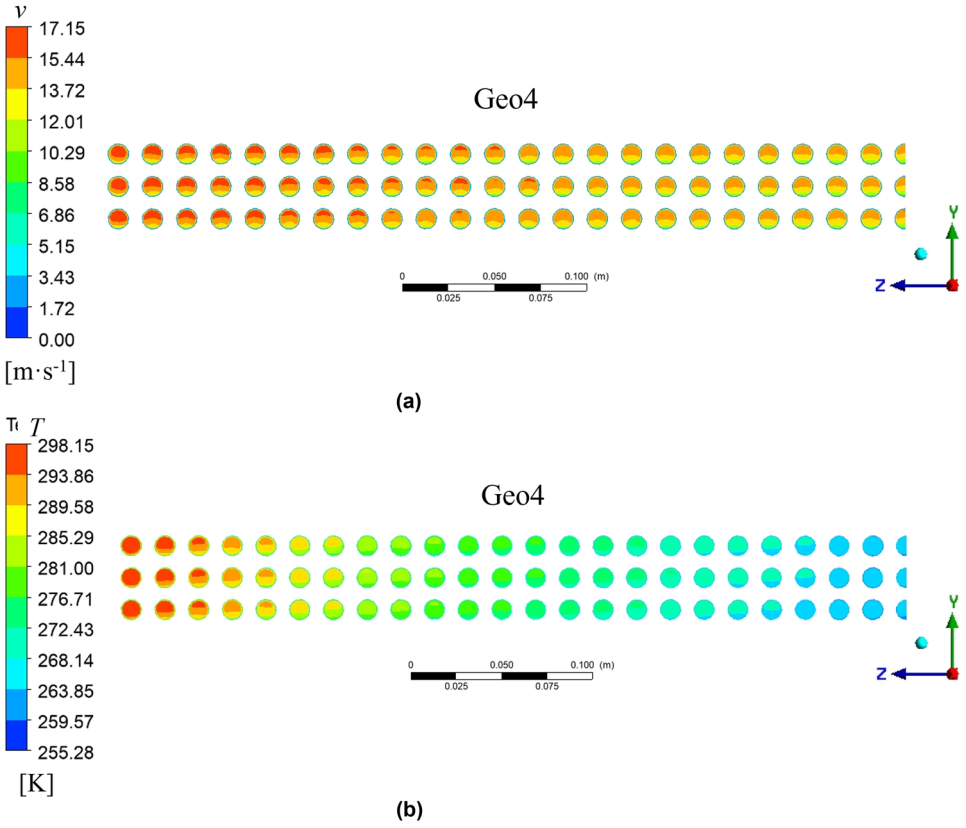

Figure 7: (a) Velocity and (b) temperature distributions in a tube with d_o = 16 mm.

Table 3: Geometric models of the core with different cylinder diameters

Parameters	Geo1	Geo2	Geo3	Geo4
d_o (mm)	16	16	16	16
D_c (mm)	70	140	210	280
P_l (mm)	19	19	19	19
P_r (mm)	18	18	18	18
β (°)	13.50	8.77	6.49	5.14

3 Result and discussion

3.1 Effect of outer diameter of HEB

The change in outer diameter of the HEB will affect the shell-side flow space and the winding angle of the tube bundle. Table 2 lists four geometric models of the outer diameter of HEB, which aim to explore the influence of the outer diameter of the winding round tubes on the thermal-hydraulic performance of the natural gas mixture on the pipe and shell sides while other structural parameters are invariant.

Figure 5 shows the variation in Nu and Δp_m on tube and shell sides with different external tube diameters. As the diameter of HEB increased from 10 to 16 mm, the Nusselt number on both sides increased linearly. This is because the winding angle of HEB gradually increases with the larger pipe diameter, which results in a stronger centrifugal force acting on the fluid inside the tubes, leading to higher secondary flow intensity and enhanced heat transfer. However, the throttling effect of the working fluid on the shell side is intensified, which strengthens the disturbance. As the tube diameter increases, there is a noticeable decrease in the pressure drop per unit length on the pipe side, with the value dropping from 3.83 kPa m^{-1} for a 10 mm tube to 1.64 kPa m^{-1} for a 16 mm tube. A large tube diameter results in greater flow resistance on the shell side, and the pressure drop per unit length increases 1.8 times when the tube diameter increases from 10 to 16 mm. This is due to the enlargement of the outer diameter of the pipe, resulting in a gradual decrease in the ratio of the shell side flow area to the radial cross-sectional area and an intensifying effect of the shell-side channel being large and small and local resistance being enhanced.

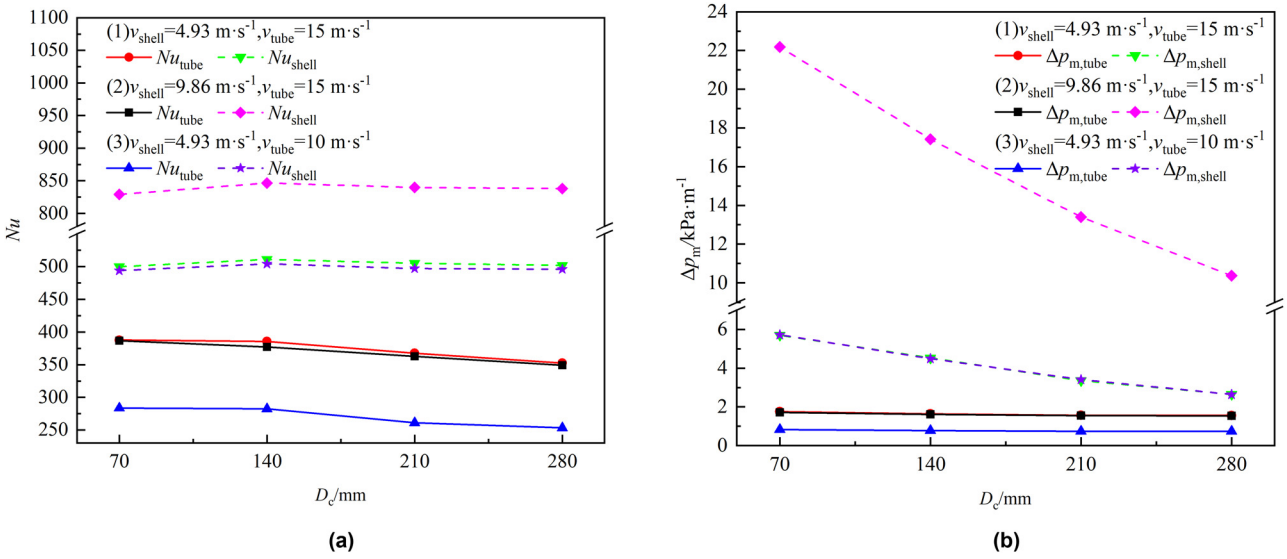

Figure 8: (a) Nu and (b) Δp_m on tube and shell sides with different core cylinder diameters.

The shell side flow area in the $y > 0$ part of the XZ section of the heat exchanger is taken. Figure 6 shows the velocity distribution on the shell side of this section in four pipe diameter structures under the working conditions v_{shell} is 4.93 m s^{-1} and v_{tube} is 15 m s^{-1}. As the heat exchange tube diameter increases, it becomes evident that the flow space for the working medium on the shell side decreases, resulting in a throttling effect between the narrow-wound tube bundles. The maximum flow velocity in the YZ section exhibits a gradual increase, starting from 20.73 m s^{-1} with a 10 mm outer diameter and reaching 20.92, 22.90, and 24.34 m s^{-1}. This trend is attributed to the diverting effect of the larger pipe diameter on the working medium on the shell side, leading to increased radial flow intensity between the heat exchange tubes in the same layer. As a result, the area of low-speed retention after HEB is reduced, the velocity within the low-flow zone rises, and the velocity distribution becomes more uniform.

Table 4: Geometric models with different longitudinal pitches

Parameters	Geo1	Geo2	Geo3	Geo4	Geo5
d_o (mm)	16	16	16	16	16
D_c (mm)	140	140	140	140	140
P_l (mm)	19	20	21	22	25
P_r (mm)	18	18	18	18	18
β (°)	8.77	9.22	9.68	10.13	11.48

Figure 7 shows the velocity and temperature distributions in a tube with an outer diameter of 16 mm. Due to the different centrifugal force at each point during the fluid flow in the tube, the high-speed region of working fluid inside the tube moves to the outside of the tube bundle at $x = 0$ section. As the working fluid inside the tube carries out heat along the spiral fluid channel, the high temperature area of the working fluid gradually moves to the

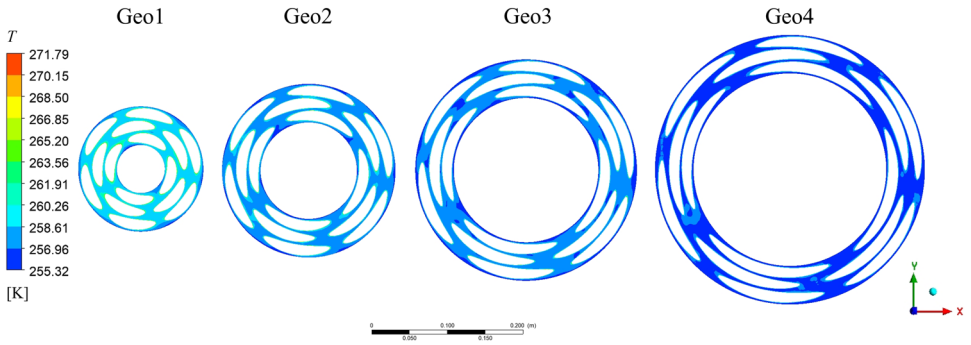

Figure 9: Temperature distribution of the shell side at the cross section of z = 250 mm with different core cylinder diameters.

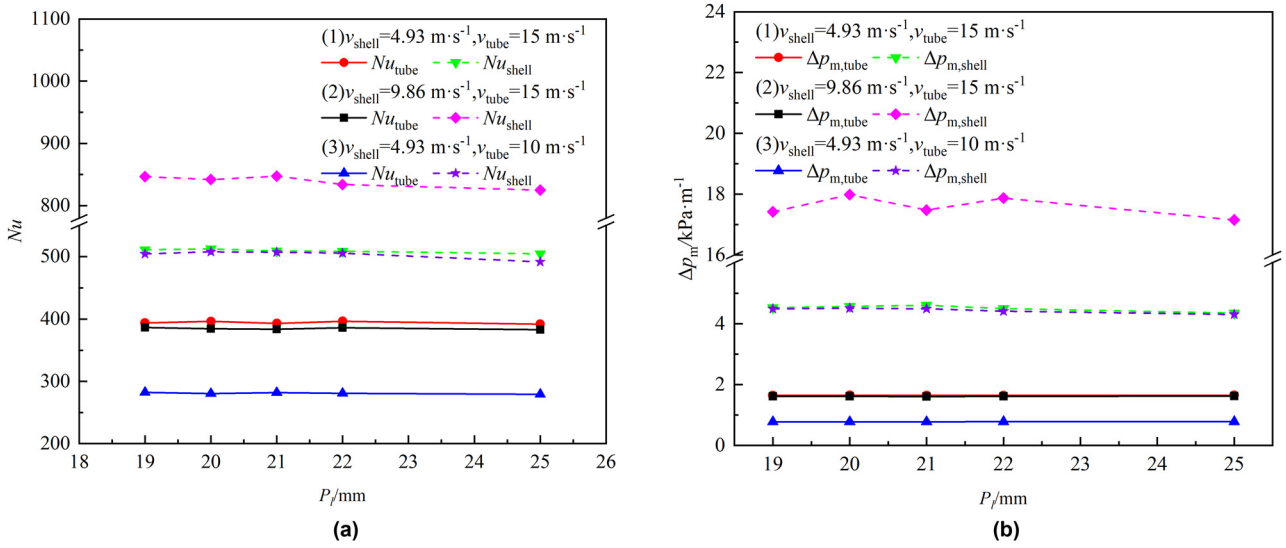

Figure 10: (a) Nu and (b) Δp_m on tube and shell sides with different longitudinal pitches.

outside of the tube bundle. Meanwhile, the low temperature area (285.2–293.8 K) is mainly concentrated in the center and inside of the tube, and the temperature displays a skewness distribution rather than a concentric circle distribution, which is one of the significant characteristics of the spiral tube, different from the straight pipe.

3.2 Effect of core tube diameter

In this study, the impacts of various barrel diameters, as detailed in Table 3, were explored. Figure 8 depicts the variation curves of Nu and Δp_m of tube on the tube and shell sides for different core tube diameters. When the

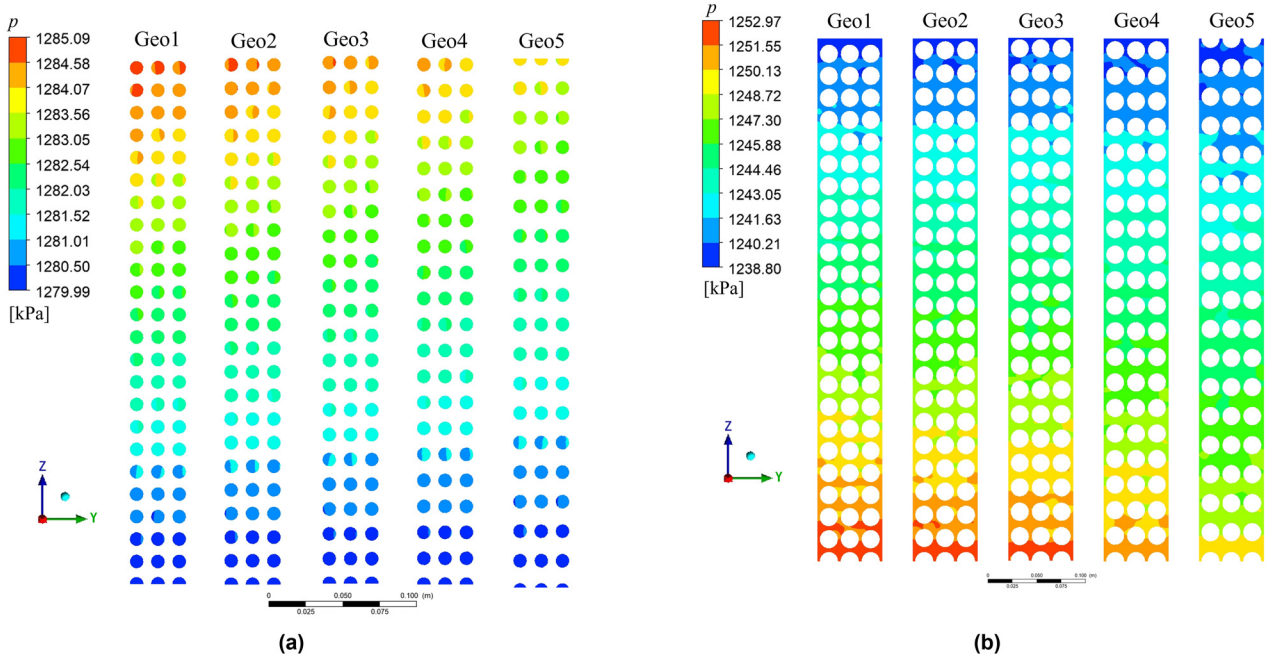

Figure 11: Pressure distribution of (a) tube and (b) shell sides on the *YZ* section with different longitudinal pitches.

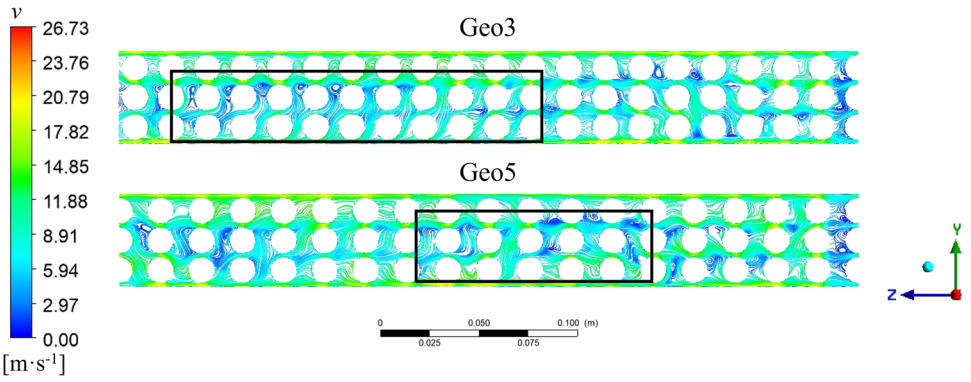

Figure 12: Streamlines on the shell side of the geometric models with P_l = 22 and 25 mm.

diameter of the core tube is reduced from 280 to 70 mm, the overall winding angle of the heat transfer tube increases from 5.14° to 13.50°, which strengthens the fluid turbulence in the tube. With the decrease in the core barrel, Nu on the shell side increased first and then decreased.

When velocities on the shell side and tube side are 4.93 and 15 m s^{-1}, the tube-side Δp_m decreases from 1.76 to 1.56 kPa m^{-1} as the diameter of the core barrel increases from 70 to 280 mm, while Δp_m on the shell side decreases from 5.71 to 2.65 kPa m^{-1}. The reason is that the smaller diameter of the core barrel increases the spiral winding angle of HEB, which results in a better conductivity effect on the shell side working medium. When the winding angle is large enough (90°), the flow of shell-side fluid between the winding tube bundles is longitudinal scouring along the tube bundles, and the pressure drop is small. Furthermore, with a higher mass flow rate of the working medium on the shell side, the impact of the core barrel diameter on the Δp_m on the shell side becomes more pronounced.

The XY cross section (z = 250 mm) was selected to observe the local temperature distribution of fluid heat transfer on the shell side. Figure 9 illustrates the temperature distribution on the shell side at the cross-section position with various core barrel diameters. Heat transfer between the core wall and the innermost heat exchange tube, as well as between the outer wall of the shell and the outermost tube bundle, is relatively ineffective. As the diameter of the core barrel decreases, the contact between the shell fluid and the tube bundle becomes more complete. When the overall fluid temperature in this section increases from 256.14 K (D_c = 280 mm) to 260.26 K (D_c = 70 mm), the heat transfer between the outer wall of the cylinder and the tube bundle is enhanced, resulting in a reduction in the size of the low-temperature retention zone.

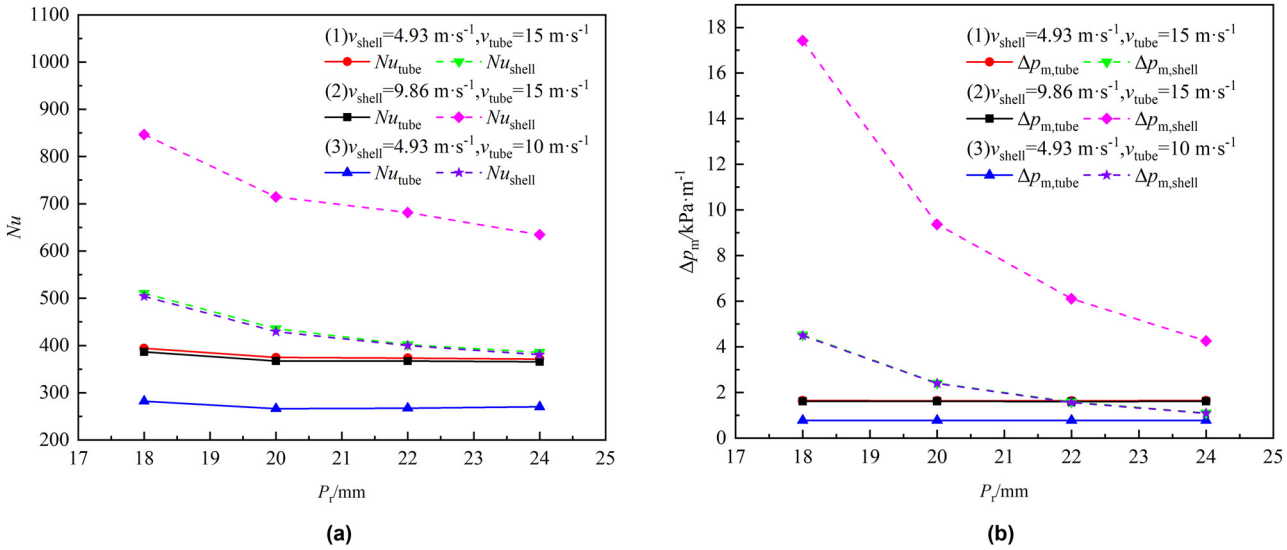

Figure 13: (a) Nu and (b) Δp_m on tube and shell sides with different radial pitches.

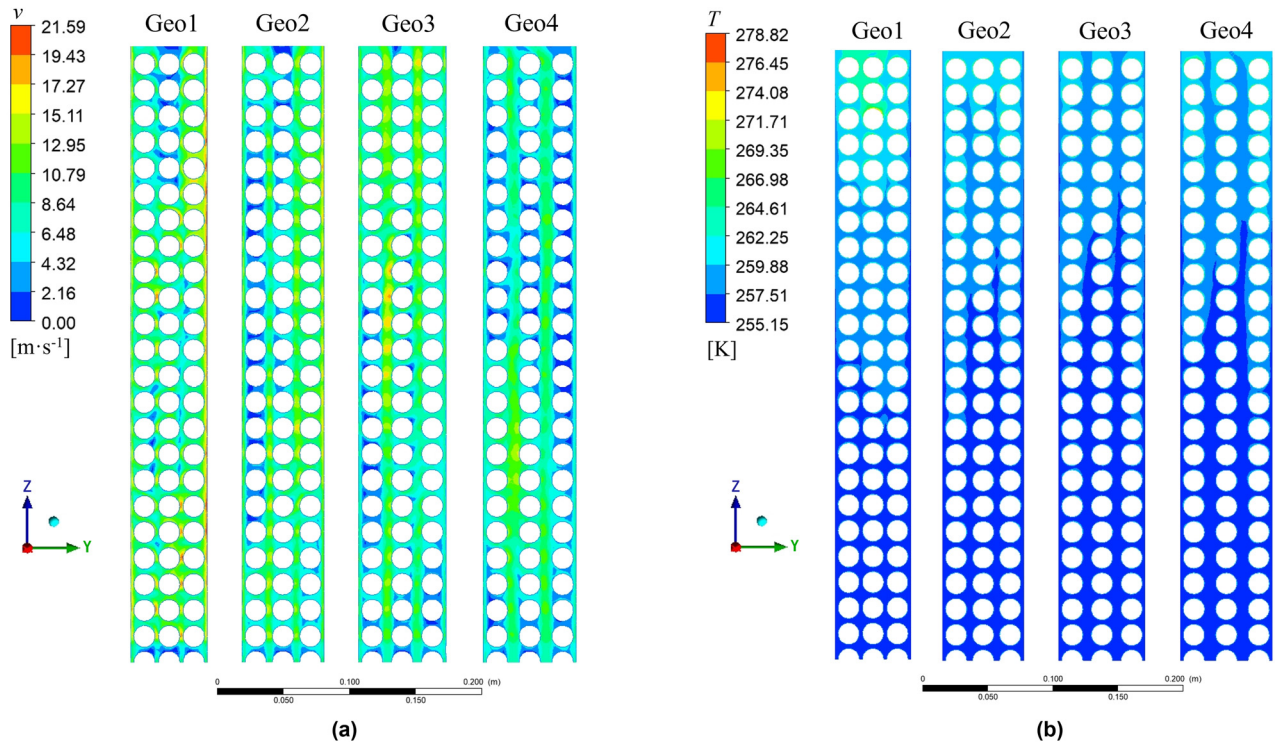

Figure 14: (a) Velocity and (b) temperature distributions of the shell side on the *YZ* section with different radial pitches.

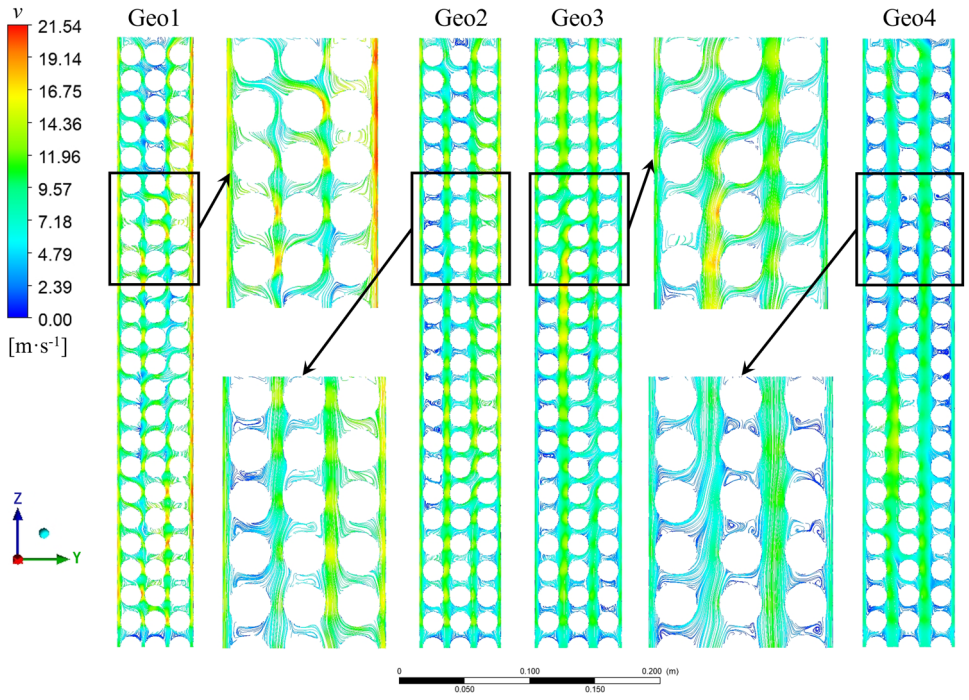

Figure 15: Streamlines of the shell side on the *YZ* section with different radial pitches.

3.3 Effect of longitudinal pitch

This work simulates five groups of heat transfer structures with different longitudinal pitch as shown in Table 4. Figure 10 presents the curves for Nu and Δp_m on both sides of the shell under various longitudinal pitches. Changes in longitudinal pitch have little impact on flow and heat transfer performance.

Figure 11(a) shows the pressure distribution of the five groups of geometric models on the *YZ* section of $x = 0$ and based on the working conditions, v_{shell} is 4.93 m s^{-1} and v_{tube} is 15 m s^{-1}. As the longitudinal pitch gradually increases, the turbulence disturbance and pressure loss caused by the large winding angle do not offset the low resistance loss caused by the shortening of effective heat transfer length. Hence, the overall pressure loss of the fluid in the pipe decreases with the increase in longitudinal pitch, and the lateral pressure loss decreases monotonically with the increase in longitudinal spacing. In addition, Figure 11(b) shows the cloud map of pressure variations on the lower shell side with varying longitudinal spacing. As the longitudinal pitch increases, the diversion effect of the tube bundle on the shell side fluid is strengthened, and the pressure loss decreases monotonically. Nevertheless, under the same coaxial heat transfer height, the length of HEB is inversely proportional to the longitudinal pitch. Thus, the pressure drop of the unit tube length shows a monotonic change different from the overall pressure loss.

Under the working conditions, v_{shell} is 4.93 and v_{tube} is 15 m s^{-1}, the turbulent energy on the lower shell side of the structure with P_l in the range of 19–25 mm were 0.47, 0.48, 0.47, 0.41, and 0.38 m^2 s^{-2}, respectively. The turbulent energy on the shell side increased first and then decreased, which was consistent with the variation trend of *Nu*. Additionally, since the longitudinal pitch is too high, the gap of HEB in the same layer will increase, which weakens the extrusion throttling effect of shell side fluid. As shown in Figure 12, streamlines of shell-side working medium with P_l are 22 and 25 mm, respectively, demonstrating that a large area of low-speed vortex zone is formed behind the tube, resulting in poor heat transfer performance.

3.4 Effect of radial pitch

Figure 13 illustrates the trends in the Nu and Δp_m on both the tube and shell sides of the spiral wound tube heat exchanger, considering radial pitches ranging from 18 to 24 mm, respectively. As the radial pitch increases, Nu on the tube side exhibits a decrease, followed by a leveling off. Nu reached its maximum value at 18 mm and slightly decreased in the range of 20–24 mm. At the same time, the pressure drops per unit length on the tube side remained relatively constant throughout the study range, with fluctuations staying within the range of 0.02 kPa m^{-1}. This is because the change in the radial pitch of the four groups is very weak compared with the overall size of the radial direction of the heat exchanger, and the overall winding angle of the spiral-wound tube bundle is less than 0.5°, which leads to a weak effect on the turbulence degree of the fluid in the tube, and the enhanced heat transfer effect is not significant so that the Nu within the radial spacing range of 20–24 mm exhibits minimal variation. Furthermore, while the difference in heat transfer intensity on the shell side can affect the tube wall temperature and fluid properties inside the tube, it has a minimal impact on the flow and heat transfer of the gas-phase working fluid in the natural gas mixture.

Figure 14 depicts the velocity and temperature distributions of the shell-side fluid on the *YZ* section of $x = 0$ in a geometric model with 18–22 mm radial spacing. Increasing the pipe layer spacing significantly increases the flow cross-sectional area of the shell side, and the throttling effect of working fluid flowing through the narrow area of the pipe layer is weakened. The turbulent kinetic energy is 0.48, 0.37, 0.27, and 0.19 m^2 s^{-2}, respectively. The average flow velocity between pipe layers decreased, which inhibited the enhancement of heat transfer. The outlet temperature of the shell side decreases from 264.7 K under the 18 mm condition to 260.1 K under $P_r = 24$ mm, and the local flow resistance decreases accordingly. The high radial pitch reduces the axial linear flow resistance between tube layers, and the fluid tends to flow directly out of the shell without fully contacting the tube bundle for heat transfer. And the low-speed retention zone behind the heat exchange tube is large, which is also reflected in the flow diagram of the working medium on the shell side (Figure 15). In the geometry structure with an 18–22 mm radial pitch, the radial flow of shell side fluid is more intense than that of $P_r = 24$ mm, and the average radial flow velocity of the *YZ* section is 0.50, 1.83, 0.93, and 0.17 m s^{-1}, respectively.

4 Conclusion

This study constructs a three-dimensional numerical model of SWHE. Four key structural parameters are investigated to find their effect on the flow and heat transfer performance of natural gas. The conclusions are as follows:

1) The outside diameter of the tube, the core tube diameter, and the radial pitch have larger effects on the performance of convection heat transfer, which should be taken as the main factors to consider in the design optimization of SWHE. Both Nu on both sides and Δp_{m} on the shell side increased with the increase in the tube diameter.
2) The longitudinal pitch shows little influence on the thermal-hydraulic characteristics, and the longitudinal pitch corresponding to the maximum values of Nu and Δp_{m} on both sides increases with the increase in *Re*.
3) The velocity and temperature fields of the fluid in the spiral-wound tube show skewness distribution under centrifugal force. The fluid in the gap between the shell wall and the innermost/outer tube bundle tends to flow out of the heat exchanger at high speed along the wall without sufficient heat exchange with the tube bundle.

Funding information: The authors state no funding involved.

Author contributions: All authors have accepted responsibility for the entire content of this manuscript and approved its submission.

Conflict of interest: The authors state no conflict of interest.

References

[1] Kanbur BB, Xiang LM, Dubey S, Choo FH, Duan F. Cold utilization systems of LNG: A review. Renew Sust Energ Rev. 2017;79:1171–88.
[2] Zheng D, Yao J, Wang J, Yin C. Optimizing photothermal conversion efficiency in a parabolic trough direct absorption solar collector through ferrofluid and magnetic field synergy. Energ Convers Manage. 2023; 285:117020.
[3] Lim W, Choi K, Moon I. Current status and perspectives of liquefied natural gas (LNG) plant design. Ind Eng Chem Res. 2013;52(9):3065–88.
[4] Jian GP, Wang SM, Sun LJ, Wen J. Numerical investigation on the application of elliptical tubes in a spiral-wound heat exchanger used in LNG plant. Int J Heat Mass Transf. 2019;130:333–41.
[5] Chen B, Zhang Y, Li L, Zhang Z, Zhang P. Application prospect analysis of plate-fin heat exchanger and pipe-wound heat exchanger in FLNG device. Petro Chem Equip. 2022;25(12):110–1.
[6] Chen B, Zhang Y, Li L, Zhang Z, Zhang P. Application prospect analysis of plate-fin heat exchanger and spiral wound heat exchanger in FLNG unit. Petro Chem Equip. 2022;25(12):110–1.
[7] Lei Z, Bao Z. Experimental investigation on laminar heat transfer performances of RP-3 at supercritical pressure in the helical coiled tube. Int J Heat Mass Transf. 2022;185:122326.
[8] Santini L, Cioncoloni A, Butel MT, Ricotti ME. Flow boiling heat transfer in a helically coiled steam generator for nuclear power applications. Int J Heat Mass Transf. 2016;92:91–9.
[9] Wu J, Li Z, Li S, Chen Y, Liu S, Xia C, et al. Numerical simulation research on two-phase flow boiling heat transfer in helically coiled tube. Nucl Eng Des. 2022;395:111827.
[10] Wu J, Tang Z, Zhu Y, Li X, Wang H, Shi Q. Two-phase secondary flow characteristics and heat transfer mechanism during boiling in a vertical helically coiled tube. Int Commun Heat Mass. 2022; 138:106398.
[11] Chang F Hu H, Shang Y, Hu Y, Li X, Lei H, et al. Experimental and numerical study on the heat transfer characteristic of supercritical water with high mass velocity in a helically coiled tube. Int J Heat Mass Transf. 2022;197:123320.
[12] Chang F, Liu Y, Lou J, Shang Y, Hu H, Li H. Experimental investigation on flow boiling heat transfer characteristics of water and circumferential wall temperature inhomogeneity in a helically coiled tube. Chem Eng Sci. 2023;272:118592.
[13] Jayakumar J, Mahajani SM, MandalL JC, Vijayan PK, Bhoi R. Experimental and CFD estimation of heat transfer in helically coiled heat exchangers. Chem Eng Res Des. 2008;86(3):221–32.
[14] Mirgolbabaei H, Taherian H, Domairry G, Ghorbani N. Numerical estimation of mixed convection heat transfer in vertical helically coiled tube heat exchangers. Int J Numer Meth Fluids. 2011;66(7):805–19.
[15] Genić SB, Jaćimović BM, Jarić MS, Budimir NJ, Dobrnjac MM. Research on the shell-side thermal performances of heat exchangers with helical tube coils. Int J Heat Mass Transf. 2012;55(15–16):4295–300.
[16] Lu X, Du XP, Zhang S, Zeng M, Wang Q. Experimental and numerical investigation on shell-side performance of multilayer spiral wound heat exchangers. Chem Eng Trans. 2013;35:445–50.
[17] Haskins A, Ei G. CFD analyses and correlation of pressure losses on the shell-side of concentric, helically-coiled tubes heat exchangers. Nucl Eng Des. 2016;305:531–46.
[18] Zachár A. Investigation of natural convection induced outer side heat transfer rate of coiled-tube heat exchangers. Int J Heat Mass Transf. 2012;55(25–26):7892–901.
[19] Ding C, Hu H, Ding G, Chen J, Mi X, Yu S, et al. Experimental investigation on downward flow boiling heat transfer characteristics of propane in shell side of LNG spiral wound heat exchanger. Int J Refrig. 2017;84:13–25.
[20] Ding C, Hu H, Ding G, Chen J, Mi X, Yu S, et al. Experimental investigation on pressure drop characteristics of two-phase hydrocarbon mixtures flow in the shell side of LNG spiral wound heat exchangers. Appl Therm Eng. 2017;127:347–58.
[21] Wu Z, Wang H, Cai W, Jiang Y. Numerical investigation of boiling heat transfer on the shell-side of spiral wound heat exchanger. Heat Mass Transf. 2016;52(9):1973–82.
[22] Neeraas BO, Fredheim AO, Aunan B. Experimental data and model for heat transfer, in liquid falling film flow on shell-side, for spiral-wound LNG heat exchanger. Int J Heat Mass Transf. 2004;47(14–16):3565–72.
[23] Bays GS, Mcadams WH. Heat transfer coefficients in falling film heater streamline flow. Ind Eng Chem. 1937;29(11):1240–6.